Top Curr Chem (2014) 347: 235–258
DOI: 10.1007/128_2014_529

Published online: 20 March 2014

Optical Response of Extended Systems Using Time-Dependent Density Functional Theory

S. Sharma, J.K. Dewhurst, and E.K.U. Gross

Abstract In this chapter, time-dependent density functional theory is introduced and an outline of the Runge–Gross theorem is presented. An equation for linear response within time-dependent density functional theory is derived. A key ingredient of this equation is the exchange-correlation kernel for which several modern-day approximation exist. These approximations are investigatead for their ability to capture the excitonic physics in absorption and electron loss spectra. To this end, results for medium (Si and diamond) to large (LiF and Ar) band-gap insulators are presented, which exhibit excitonic physics to varying degrees.

Keywords Bootstrap kernel · Dielectric function · Excitons exchange-correlation kernel · Linear response · Optical excitations · Runge–Gross theorem · TDDFT

Contents

S. Sharma (✉), J.K. Dewhurst, and E.K.U. Gross
Max-Planck-Institut für Mikrostrukturphysik, Weinberg 2, 06120 Halle, Germany
e-mail: sharma@mpi-halle.mpg.de

TH-2014-38

1 Introduction

Given that the particles we intend to study are electrons interacting via the Coulomb potential, the exact procedure would be to solve the many-body Schrödinger equation to obtain the many-body wavefunction $\Phi(\mathbf{r}_1, \mathbf{r}_2 \ldots \mathbf{r}_N)$. This wavefunction is an enormous object which depends on the coordinates of all N electrons in the system under investigation. To store this object for, say, the Ne atom in three dimensions by just dividing the entire space into 100 points in each direction, would require more computer storage than is available in the world, indicating that it is impossible to store, let alone manipulate such an object. However, this many-body wavefunction contains far more information than is needed in any practical terms and, as was shown by Hohenberg and Kohn [1] in their work on density functional theory (DFT), one requires only the electron density to describe the ground-state properties of a many-electron system. In other words, the ground-state and all observables are unique functionals of the electron density alone. DFT can be formulated in the Kohn–Sham (KS) approach [2] where an efficient one-particle non-interacting Kohn–Sham equation yields non-interacting eigenvalues and orbitals which can be used to construct the fully interacting density of the system. In this case, the complication of the problem is hidden in the exchange and correlation (xc) potential $v_{\mathrm{xc}}[\rho](\mathbf{r})$ that appears in the Kohn–Sham equation and is an *unknown* functional of the density. Several approximations for this functional have been proposed and are known to give accurate results for the ground-state properties of the system [3]. Static DFT in conjunction with efficient xc functionals [2, 4–7] is regularly used as a predictive theory for ground-state properties of materials.

There are certain classes of systems, like strongly correlated materials [8] or those which are van der Waals bonded [9], where most of the approximate xc functionals within DFT fail. However, even with the *exact* static ground-state functional, DFT cannot be used to describe electronic excitations – for example, the optical response of a system. This is not a question of the available approximations: even if one could calculate the exact Kohn–Sham eigenvalues, their differences would not necessarily be close to measured excitation energies. As a matter of principle, they neither stand for electron addition or removal energies [10] nor do they represent optical (neutral) excitation energies. Such optical excitation embodies the response of materials to visible light. From the point of view of the theory, this light is represented by a time-dependent vector potential – a good approximation when the incident flux of photons is large. Accurate ab initio calculations of optical absorption spectra of this type would involve two steps. First, the quasi-particle spectral density function is calculated using

the *GW* approximation [11], yielding accurate electron removal and addition energies, and therefore a good prediction for the fundamental gap. In the second step, the Bethe–Salpeter equation (BSE) [12] is solved using the one-body Green's function obtained in the *GW* step. Resonances, corresponding to bound electron–hole pairs called excitons, which have energies inside the gap, can then appear in the spectrum. The two-step procedure described above is the current gold standard for obtaining optical spectra of solids. Unfortunately, both the *GW* approximation and the BSE are computationally expensive, involving manipulations of very large matrices.

Time-dependent density functional theory (TDDFT) [13–17], which extends density functional theory into the time domain, is another method able, in principle, to determine exact neutral excitations of a system. In this chapter we describe the basic theorems of TDDFT and demonstrate how optical excitation spectra can be obtained with the linear response form of TDDFT.

2 Runge–Gross Theorem

The ground-state formulation of DFT, which states that there is a one-to-one correspondence between densities and potentials, is a direct consequence of the Rayleigh–Ritz minimum principle for total energy [1, 2, 18, 19]. A straightforward extension of the Hohenberg–Kohn theorem based on this principle to the time-dependent case is not possible due to the lack of an energy minimum principle – the presence of a time-dependent external potential implies that the energy is not conserved. Nevertheless, a one-to-one correspondence between time-dependent densities and potentials can be established and this was originally done by Runge and Gross [13]. In the following we sketch this proof.

The time evolution of a (non-relativistic and spin unpolarized) system of N interacting electrons is governed by the time-dependent Schrödinger equation (atomic units are used everywhere):

$$i\frac{\partial}{\partial t}\Phi(\mathbf{r}_1, \mathbf{r}_2 \ldots \mathbf{r}_N, t) = \hat{H}(\{\mathbf{r}\}, t)\mathbf{\Phi}(\mathbf{r}_1, \mathbf{r}_2 \ldots \mathbf{r}_N, t), \quad \mathbf{\Phi}(t_0) \quad \text{given}, \tag{1}$$

where $\hat{H}(\{\mathbf{r}\}, t)$ is the Hamiltonian operator which can be written as

$$\hat{H}(\{\mathbf{r}\}, t) = \sum_{i=1}^{N}\left[-\frac{1}{2}\nabla_i^2 + v_{\text{ext}}(\mathbf{r}_i, t)\right] + \frac{1}{2}\sum_{i\neq j}^{N}\frac{1}{|\mathbf{r}_i - \mathbf{r}_j|}, \tag{2}$$

where the first term on the right-hand-side is the one-particle kinetic energy and $v_{\text{ext}}(\mathbf{r}, t)$ is the time-dependent external potential. The one electron density of this system is given by

$$\rho(\mathbf{r}, t) = N\int d^3r_2 \ldots \int d^3r_N \left|\Phi(\mathbf{r}, \mathbf{r}_2, \ldots \mathbf{r}_N, t)\right|^2. \tag{3}$$

The Runge–Gross theorem [13] states that if two time-dependent external potentials $v_{\text{ext}}(\mathbf{r}, t)$ and $v'_{\text{ext}}(\mathbf{r}, t)$ differ by more than a purely time-dependent function, then the associated time-dependent densities, $\rho(\mathbf{r}, t)$ and $\rho'(\mathbf{r}, t)$, must be different. In order to establish this one-to-one correspondence between densities and potentials, two assumptions must be made – (1) only those densities are considered that evolve from a common initial state $|\Phi(t_0)\rangle$ (this initial state need not be the ground-state or an eigenstate of the initial potential, $v_{\text{ext}}(\mathbf{r}, t_0)$) and (2) the class of potentials is restricted to those which can be Taylor expanded around the initial time, t_0:

$$v_{\text{ext}}(\mathbf{r}, t) = \sum_{i=0}^{\infty} \frac{1}{i!} u_i(\mathbf{r})(t - t_0)^i, \tag{4}$$

where $u_i(\mathbf{r})$ are the Taylor coefficients of this expansion.

Since both external potentials are assumed to be expandable in a Taylor series and differ by more than a purely time-dependent function, some of the expansion coefficients $u_i'(\mathbf{r})$ and $u_i'(\mathbf{r})$ differ by more than a constant and as a result there exists a smallest index $k \geq 0$ such that

$$u_k(\mathbf{r}) - u'_{\text{k}}(\mathbf{r}) = \frac{\partial^k}{\partial t^k}[v_{\text{ext}}(\mathbf{r}, t) - v'_{\text{ext}}(\mathbf{r}, t)]\Big|_{t=t_0} \neq \text{constant}. \tag{5}$$

Using this inequality, the one-to-one mapping between external potential and density can be demonstrated in two steps. First a one-to-one mapping between external potential and current-density is established. Given this result, in the second step the continuity equation is used to relate time-derivatives of the charge-density to time-derivatives of the external potential.

2.1 Step 1: One-to-One Mapping Between Current-Density and External Potential

The current density $\mathbf{j}(\mathbf{r}, t)$ is given by

$$\begin{aligned}\mathbf{j}(\mathbf{r},t) = &-\frac{i}{2}N\int d^3r_2 \ldots \int d^3r_N \Phi^*\left(\mathbf{r},\mathbf{r}_2,\ldots\mathbf{r}_N,t\right)[\nabla\Phi(\mathbf{r},\mathbf{r}_2,\ldots\mathbf{r}_N,t)] \\ &-[\nabla\Phi^*(\mathbf{r},\mathbf{r}_2,\ldots\mathbf{r}_N,t)]\Phi\left(\mathbf{r},\mathbf{r}_2,\ldots\mathbf{r}_N,t\right) \\ &= -\frac{i}{2}\left\langle\Phi(t)\middle|\hat{\psi}^\dagger(\mathbf{r})[\nabla\hat{\psi}(\mathbf{r})] - \left[\nabla\hat{\psi}^\dagger(\mathbf{r})\right]\hat{\psi}(\mathbf{r})\middle|\Phi(t)\right\rangle = \left\langle\Phi(t)\middle|\hat{\mathbf{j}}(\mathbf{r})\middle|\Phi(t)\right\rangle.\end{aligned} \tag{6}$$

The time evolution of this current-density is given by the equation of motion:

$$i\frac{\partial}{\partial t}\mathbf{j}(\mathbf{r},t) = \left\langle \Phi(t)\middle|\left[\hat{\mathbf{j}}(\mathbf{r}), \hat{H}(\{\mathbf{r}\},t)\right]\middle|\Phi(t)\right\rangle. \tag{7}$$

By subtracting the equations of motion for two different current densities $\mathbf{j}(\mathbf{r}, t)$ and $\mathbf{j}'(\mathbf{r}, t)$ we obtain:

$$\frac{\partial}{\partial t}[\mathbf{j}(\mathbf{r},t) - \mathbf{j}'(\mathbf{r},t)]\Big|_{t=t_0} = \rho(\mathbf{r},t_0)\nabla[v_{\text{ext}}(\mathbf{r},t) - v'_{\text{ext}}(\mathbf{r},t)]|_{t=t_0}. \tag{8}$$

If the condition in (5) is satisfied for $k = 0$, the right-hand-side of (8) cannot vanish identically, and hence the currents become different at times infinitesimally later than t_0. If (5) is satisfied for $k > 0$, one can take an appropriate higher derivative by repeatedly using the equation of motion to obtain

$$\frac{\partial^{k+1}}{\partial t^{k+1}}[\mathbf{j}(\mathbf{r},t) - \mathbf{j}'(\mathbf{r},t)]\Big|_{t=t_0} = \rho(\mathbf{r},t_0)\nabla\frac{\partial^k}{\partial t^k}[v_{\text{ext}}(\mathbf{r},t_0) - v'_{\text{ext}}(\mathbf{r},t_0)]\Big|_{t=t_0}. \tag{9}$$

This equation shows that even for $k > 0$ the current densities evolve differently in time for $t > t_0$, establishing the one-to-one correspondence between the current density and the external potential.

2.2 *Step 2: One-to-One Mapping Between Current Density and Charge Density*

So far it has been established that the current densities arising from two different external potentials are different. Based on this, it can also be demonstrated that the corresponding charge-densities are different – this can be done using the continuity equation, which is a consequence of the conservation of total particle number, and establishes the relation between the time-dependent charge- and current-density:

$$\frac{\partial}{\partial t}\rho(\mathbf{r},t) = -\nabla\cdot\mathbf{j}(\mathbf{r},t), \tag{10}$$

and, together with (9), this gives

$$\frac{\partial^{k+2}}{\partial t^{k+2}}\Big[\rho(\mathbf{r},t)-\rho'(\mathbf{r},t)\Big]\Big|_{t=t_0} = -\nabla\cdot\frac{\partial^{k+1}}{\partial t^{k+1}}\Big[\mathbf{j}(\mathbf{r},t)-\mathbf{j}'(\mathbf{r},t)\Big]\Big|_{t=t_0}$$
$$= -\nabla\cdot\left\{\rho(\mathbf{r},t_0)\nabla\frac{\partial^k}{\partial t^k}[v_{\text{ext}}(\mathbf{r},t)-v'_{\text{ext}}(\mathbf{r},t)]\Big|_{t=t_0}\right\}. \tag{11}$$

If the right-hand-side of this equation is non-zero, the $(k + 2)$th term in the Taylor expansion of the two densities is different, making the two densities different for $t > t_0$.

In order to show that the right-hand-side of (11) is indeed non-zero provided that (5) is satisfied, one first writes

$$\int d^3r f(\mathbf{r})\nabla\cdot[\rho(\mathbf{r},t_0)\nabla f(\mathbf{r})] = \int d^3r\nabla\cdot[f(\mathbf{r})\rho(\mathbf{r},t_0)\nabla f(\mathbf{r})]$$
$$-\int d^3r\rho(\mathbf{r},t_0)\big|\nabla f(\mathbf{r})\big|^2, \tag{12}$$

where $f(\mathbf{r}) = \partial^k[v_{\text{ext}}(\mathbf{r},t) - v'_{\text{ext}}(\mathbf{r},t)]/\partial t^k\big|_{t=t_0}$. Making use of the Green's identity this can be written as

$$\int d^3r f(\mathbf{r})\nabla\cdot[\rho(\mathbf{r},t_0)\nabla f(\mathbf{r})] = \int[f(\mathbf{r})\rho(\mathbf{r},t_0)\nabla f(\mathbf{r})]\cdot d\mathbf{s}$$
$$-\int d^3r\rho(\mathbf{r},t_0)\big|\nabla f(\mathbf{r})\big|^2, \tag{13}$$

The first term on the right-hand-side is a surface integral at $\mathbf{r} = \infty$ which vanishes for all finite, real-world systems, i.e., systems whose densities fall off to zero exponentially, and whose potentials may increase asymptotically at most with a power law. If $\nabla f(\mathbf{r})$ is non-zero somewhere the second term on the right-hand side is non-zero. Thus it is impossible for $\nabla f(\mathbf{r})$ to be non-zero and, at the same time, $\nabla(\rho(\mathbf{r})\nabla f(\mathbf{r}))$ to be zero everywhere.

To summarize the Runge–Gross theorem (also see [20–22]) – for two external time-dependent potentials, which differ by more than a purely time-dependent function, the time-dependent densities evolving from a common initial state under the influence of these two different potentials are different. Hence, the time-dependent density uniquely determines the time-dependent potential up to a purely time-dependent function. Since the effect on the wavefunction of adding a purely time-dependent function to the external potential is an additional time-dependent phase factor, which cancels on taking an expectation value, we see that each observable is also a unique functional of the time-dependent density. It should be noted that the one-to-one correspondence between potentials and densities holds true for any fixed initial state, but the mapping depends on the initial state. However, for a system *evolving from its ground-state*, the initial state itself is, by virtue of the

Hohenberg–Kohn theorem [1], a functional of the ground-state density, and hence this dependence on the initial state can be lifted.

3 Time-Dependent Kohn–Sham Equations

The Runge–Gross theorem states that the time-dependent density is the central quantity and all observables can, in principle, be determined from just knowing the density, but it does not give a prescription as to how this density can be evaluated. To provide such a prescription, within static DFT, Kohn and Sham suggested [2] the use of an auxiliary non-interacting system of electrons moving in an effective potential such that the density of this non-interacting system is equal to the density of the full interacting system. A similar scheme can also be used within TDDFT; having established that the external potential is a unique functional of the initial state and the density, a system of non-interacting particles is chosen such that the density of this non-interacting system is equal to that of the interacting system *for all times* [13]. The advantage of doing so lies in the ease with which non-interacting systems can be solved – the wavefunction of this non-interacting system can be represented as a Slater determinant of single-particle orbitals, which are determined by solving the time-dependent Kohn–Sham equations:

$$i\frac{\partial \psi_j(\mathbf{r},t)}{\partial t} = \left[-\frac{\nabla^2}{2} + v_0(\mathbf{r},t) + v_{\mathrm{H}}[\rho](\mathbf{r},t) + v_{\mathrm{xc}}[\rho](\mathbf{r},t)\right]\psi_j(\mathbf{r},t), \tag{14}$$

where the $\psi_j(\mathbf{r}, t)$ denote the single-particle Kohn–Sham orbitals whose density, $\rho(\mathbf{r}, t)$, is given by

$$\rho(\mathbf{r},t) = 2\sum_{j=1}^{N/2} \left|\psi_j(\mathbf{r},t)\right|^2. \tag{15}$$

$v_0(\mathbf{r}, t)$ is the (given) external potential that defines the problem that is to be solved. Typically $v_0(\mathbf{r}, t)$ contains the Coulomb potential of the nuclei plus a laser field. The Hartree potential has the form

$$v_{\mathrm{H}}[\rho](\mathbf{r},t) = \int d^3r' \frac{\rho(\mathbf{r}',t)}{|\mathbf{r}-\mathbf{r}'|}, \tag{16}$$

and the exchange-correlation potential, v_{xc}, has a functional dependence on the density of the system at the current and at all previous times; hence it includes the

information about the whole history of this time propagation. The exact exchange-correlation (xc) potential is a universal functional of the density and is defined by

$$v_{\mathrm{xc}}[\rho, \Phi_0, \Psi_0](\mathbf{r}, t) \equiv v_{\mathrm{s}}[\rho, \Psi_0](\mathbf{r}, t) - v_{\mathrm{ext}}[\rho, \Phi_0](\mathbf{r}, t) - v_{\mathrm{H}}[\rho](\mathbf{r}, t). \tag{17}$$

Here $v_{\mathrm{s}}[\rho, \Psi_0](\mathbf{r}, t)$ is the Runge–Gross one-to-one mapping of non-interacting particles (and Ψ_0 the initial determinant) whereas $v_{\mathrm{ext}}[\rho, \Phi_0](\mathbf{r}, t)$ is the Runge–Gross one-to-one mapping for Coulomb interacting electrons. The knowledge of this functional would solve all time-dependent (externally driven) Coulomb problems; in practice, however, the xc potential is always approximated.

4 Linear Response

One of the main aims of this book is to study electronic excitations. In this section we show that the time-dependent Kohn–Sham equations can be used to study such charge neutral excitations efficiently [23] – the system is perturbed by some weak electric field and then propagated via the time-dependent Kohn–Sham equations [24, 25]. The time-dependent current, and consequently the optical conductivity, is evaluated at each time step. The Fourier transform of this optical conductivity gives the optical absorption spectra of the system [26]. In most cases, however, when the external perturbation, $v_{\mathrm{ext}}(\mathbf{r}, t) = v^0_{\mathrm{ext}}(\mathbf{r}) + v^{(1)}_{\mathrm{ext}}(\mathbf{r}, t)$, is sufficiently small (such that it does not completely destroy the ground-state structure of the system), it is enough to calculate the linear-response of the system. The advantage to linear response is that the exact solution can be obtained using simple linear algebra operations. The first-order correction to the density, in terms of the perturbing external potential, $v^{(1)}_{\mathrm{ext}}$, is given by

$$\rho^{(1)}(\mathbf{r}, t) = \int_{-\infty}^{\infty} dt' \int d^3r' \chi(\mathbf{r}, \mathbf{r}', t - t') v^{(1)}_{\mathrm{ext}}(\mathbf{r}', t'), \tag{18}$$

where χ is the linear density-density response function of the fully interacting system

$$\chi(\mathbf{r}, \mathbf{r}', t - t') = \left. \frac{\delta \rho(\mathbf{r}, t)}{\delta v_{\mathrm{ext}}(\mathbf{r}', t')} \right|_{v_{\mathrm{ext}}(\mathbf{r}', t') = v^{(0)}_{\mathrm{ext}}(\mathbf{r}')}, \tag{19}$$

and causality implies that $\chi(\mathbf{r}, \mathbf{r}', t - t') = 0$ for $t < t'$. In order to write the full response function in terms of the linear density-density response of the non-interacting Kohn–Sham system, χ_{s}, one can use the chain rule to write

$$\chi(\mathbf{r},\mathbf{r}',t-t') = \int_{-\infty}^{\infty} dt'' \int d^3r'' \frac{\delta\rho(\mathbf{r},t)}{\delta v_s(\mathbf{r}'',t'')} \frac{\delta v_s(\mathbf{r}'',t'')}{\delta v_{ext}(\mathbf{r}',t')}$$
$$= \int_{-\infty}^{\infty} dt'' \int d^3r'' \chi_s(\mathbf{r},\mathbf{r}'',t-t'') \frac{\delta v_s(\mathbf{r}'',t'')}{\delta v_{ext}(\mathbf{r}',t')}. \quad (20)$$

The Runge–Gross theorem ensures that for any given external potential, $v_{ext}(\mathbf{r}, t)$, the corresponding Kohn–Sham potential, $v_s(\mathbf{r}', t')$, is uniquely defined. The existence of $v_s(\mathbf{r}', t')$, i.e., non-interacting v-representability, has been demonstrated in [27]. The variation of the Kohn–Sham potential ($v_s = v_{ext} + v_H + v_{xc}$) with respect to the external potential can be evaluated as

$$\frac{\delta v_s(\mathbf{r}'',t'')}{\delta v_{ext}(\mathbf{r}',t')} = \delta(\mathbf{r}''-\mathbf{r}')\delta(t''-t') + \frac{\delta v_H(\mathbf{r}'',t'')}{\delta v_{ext}(\mathbf{r}',t')} + \frac{\delta v_{xc}(\mathbf{r}'',t'')}{\delta v_{ext}(\mathbf{r}',t')}. \quad (21)$$

Since both the Hartree and xc potentials are functionals of the density, a further application of the chain rule can be used to write

$$\frac{\delta v_H(\mathbf{r}'',t'')}{\delta v_{ext}(\mathbf{r}',t')} = \int_{-\infty}^{\infty} dt''' \int d^3r''' \frac{\delta v_H(\mathbf{r}'',t'')}{\delta\rho(\mathbf{r}''',t''')} \frac{\delta\rho(\mathbf{r}''',t''')}{\delta v_{ext}(\mathbf{r}',t')}$$
$$= \int_{-\infty}^{\infty} dt''' \int d^3r''' \frac{\delta(t''-t''')}{|\mathbf{r}''-\mathbf{r}'''|} \chi(\mathbf{r}''',\mathbf{r}',t'''-t'). \quad (22)$$

For the last term in (21) we define a new quantity, the so-called exchange-correlation kernel, f_{xc}, which is given by

$$f_{xc}(\mathbf{r}'',\mathbf{r}''',t''-t''') = \left.\frac{\delta v_{xc}(\mathbf{r}'',t'')}{\delta\rho(\mathbf{r}''',t''')}\right|_{\rho(\mathbf{r}''',t''')=\rho^{(0)}(\mathbf{r}''')}. \quad (23)$$

After collecting all the terms and inserting them in (20) one gets a Dyson-like equation for the density-density linear response function of the fully interacting system [23]. This response function can be Fourier transformed to frequency space, whereby convolutions on the time axis become simple multiplications, thus yielding the final expressions:

$$\chi(\mathbf{r},\mathbf{r}',\omega) = \chi_s(\mathbf{r},\mathbf{r}',\omega) + \int d^3r'' \int d^3r''' \chi_s(\mathbf{r},\mathbf{r}'',\omega) \left[\frac{1}{|\mathbf{r}''-\mathbf{r}'''|} + f_{xc}(\mathbf{r}'',\mathbf{r}''',\omega)\right] \chi(\mathbf{r}''',\mathbf{r}',\omega). \quad (24)$$

From this equation it is possible to extract the excitation energies of the system, as these are simply the poles of the response function. An essential ingredient of this equation is the Kohn–Sham response function, which can be calculated straightforwardly from time-dependent perturbation theory. The expression in terms of the

ground-state Kohn–Sham orbitals, $\{\psi_i\}$, their eigenvalues, $\{\epsilon_i\}$, and occupation numbers, $\{n_i\}$, reads

$$\chi_s(\mathbf{r},\mathbf{r}',\omega) = \lim_{\eta\to 0}\sum_{i=1}^{\infty}\sum_{j=1}^{\infty}\left(n_i - n_j\right)\frac{\psi_i^*(\mathbf{r})\psi_j(\mathbf{r})\psi_i(\mathbf{r}')\psi_j^*(\mathbf{r}')}{\omega - \epsilon_j + \epsilon_i + i\eta}. \tag{25}$$

4.1 Dielectric Function for Extended Systems

In this section we shall work out the linear response formalism for extended, periodic systems. For these systems, the concept of screening is a crucial ingredient. Intuitively, an applied time-dependent external perturbation polarizes the system such that the electrons screen the system from the applied perturbation. The total electrostatic potential felt by a test charge inserted into the medium is then given by

$$v_{\text{tot}}(\mathbf{r},t) = v_{\text{ext}}(\mathbf{r},t) + v_{\text{ind}}(\mathbf{r},t) = \int_{-\infty}^{\infty} dt' \int d^3r' \varepsilon^{-1}(\mathbf{r},\mathbf{r}',t-t')v_{\text{ext}}(\mathbf{r}',t'), \tag{26}$$

where we have expressed the screened potential in terms of the inverse dielectric function ε. v_{ind} is the induced potential due to the polarization of the system, i.e., the potential generated by the induced density (this potential also contains xc effects). Hence, using (18), it is related to the density–density response function as

$$v_{\text{ind}}(\mathbf{r},t) = \int_{-\infty}^{\infty} dt' \int d^3r'' \int d^3r' \frac{\chi(\mathbf{r}'',\mathbf{r}',t-t')v_{\text{ext}}(\mathbf{r}',t')}{|\mathbf{r}-\mathbf{r}''|}. \tag{27}$$

This, together with (26), leads to the following relation between the dielectric function and χ:

$$\varepsilon^{-1}(\mathbf{r},\mathbf{r}',t-t') = \delta(\mathbf{r}-\mathbf{r}')\delta(t-t') + \int d^3r'' \frac{\chi(\mathbf{r}'',\mathbf{r}',t-t')}{|\mathbf{r}-\mathbf{r}''|}. \tag{28}$$

In a perfect crystal with translational symmetry, if the coordinates are shifted by a lattice vector $\mathbf{R}$, the dielectric function stays unchanged:

$$\varepsilon(\mathbf{r}+\mathbf{R},\mathbf{r}'+\mathbf{R},t-t') = \varepsilon(\mathbf{r},\mathbf{r}',t-t'). \tag{29}$$

It is therefore most convenient to perform a Fourier transform to reciprocal space where the dielectric function is conventionally written as

$$\varepsilon(\mathbf{r},\mathbf{r}',t-t') = \frac{1}{\Omega}\sum_{\mathbf{q}}\sum_{\mathbf{G}\mathbf{G}'} e^{-i[(\mathbf{q}+\mathbf{G})\mathbf{r}-\omega(t-t')]}\varepsilon(\mathbf{q}+\mathbf{G},\mathbf{q}+\mathbf{G}',\omega)e^{i[(\mathbf{q}+\mathbf{G}')\mathbf{r}'-\omega(t-t')]} \tag{30}$$

where $\mathbf{q}$ is a vector within the first Brillouin zone, $\mathbf{G}$ and $\mathbf{G}'$ are reciprocal lattice vectors, and Ω is the volume of the crystal. In reciprocal space, the three-dimensional integral in (28) becomes a simple matrix multiplication and the inverse dielectric function reads

$$\varepsilon^{-1}\left(\mathbf{G},\mathbf{G}',\mathbf{q},\omega\right)=\delta\left(\mathbf{G}-\mathbf{G}'\right)+\sum_{G''}\frac{4\pi\delta\left(\mathbf{G}-\mathbf{G}''\right)}{\left|(\mathbf{G}+\mathbf{q})\left(\mathbf{G}''+\mathbf{q}\right)\right|}\chi\left(\mathbf{G}'',\mathbf{G}',\mathbf{q},\omega\right). \quad (31)$$

In reciprocal space, the Dyson equation (24) can be solved for the density–density response function χ yielding

$$\chi\left(\mathbf{G},\mathbf{G}',\mathbf{q},\omega\right)=\sum_{\mathbf{G}''}\left\{\left[\delta(\mathbf{G}_1-\mathbf{G}_2)-\sum_{\mathbf{G}_3}\chi_s(\mathbf{G}_1,\mathbf{G}_3,\mathbf{q},\omega)\right.\right.$$

$$\left.\left.\times\left(\frac{4\pi\delta(\mathbf{G}_3-\mathbf{G}_2)}{|(\mathbf{G}_3+\mathbf{q})(\mathbf{G}_2+\mathbf{q})|}+f_{xc}(\mathbf{G}_3,\mathbf{G}_2,\mathbf{q},\omega)\right)\right]^{-1}\right\}_{G,G''}\chi_s\left(\mathbf{G}',\mathbf{G}'',\mathbf{q},\omega\right). \quad (32)$$

The head of the dielectric tensor, also known as the macroscopic part, can be directly compared to experiments: $\left[1/\varepsilon^{-1}\left(\mathbf{G},\mathbf{G}',\mathbf{q},\omega\right)\right]_{\mathbf{G}=\mathbf{G}'=0}$ corresponds to the absorption spectra [28–31] and $\varepsilon^{-1}(\mathbf{G}=\mathbf{G}'=0,\ \mathbf{q},\ \omega)$ to the electron energy loss spectra (EELS) [32–36].

5 Exchange-Correlation Kernels and Optical Absorption Spectra

The xc kernel in (32) can be heuristically (but not uniquely) written as a sum of two terms: $f_{xc}=f_{xc}^{(1)}+f_{xc}^{(2)}$. This partition of the kernel into two parts is done to capture two different effects. (1) The band-gaps calculated using local/semilocal approximations to the xc potential within DFT are well known to be underestimated. In order to get the correct band structure one can perform a *GW* calculation. Precisely the same effect is obtained by the exact xc kernel without recourse to the many-body perturbation theory. $f_{xc}^{(1)}$ is such a kernel and is responsible for correcting the underestimated band-gap. (2) The second part of the xc kernel, $f_{xc}^{(2)}$, is responsible for capturing the excitonic physics. Equation (32) can then be written as (we suppress the $\mathbf{G}$, $\mathbf{G}'$ indices for clarity)

$$\chi(\mathbf{q},\omega)=\left[1-\chi_{gc}(\mathbf{q},\omega)\left(V_{cl}+f_{xc}^{(2)}(\mathbf{q},\omega)\right)\right]^{-1}\chi_{gc}(\mathbf{q},\omega), \quad (33)$$

where $V_{\rm cl}(\mathbf{G}, \mathbf{G}', \mathbf{q}) = 4\pi\delta(\mathbf{G} - \mathbf{G}')/|(\mathbf{G} + \mathbf{q})(\mathbf{G}' + \mathbf{q})|$ is the Coulomb potential and

$$\chi_{\rm gc}(\mathbf{q}, \omega) = \left[1 - \chi_{\rm s}(\mathbf{q}, \omega) f_{\rm xc}^{(1)}(\mathbf{q}, \omega)\right]^{-1} \chi_{\rm s}(\mathbf{q}, \omega), \tag{34}$$

is the gap corrected Kohn–Sham response function of the system. For all further calculation (TDDFT and BSE) we use for $\chi_{\rm gc}$ the simplest possible choice, namely the response function calculated from the scissor operator corrected Kohn–Sham band structure – unoccupied Kohn–Sham eigenvalues are rigidly shifted to higher energies to make the Kohn–Sham and exact fundamental band-gap equal. In order to keep the whole procedure parameter free, the value of the "exact" fundamental band-gap is calculated using the *GW* method.

Although formally exact, the predictions of optical absorption spectra from TDDFT are only as good as the approximation of the xc kernel. For example, by taking a rather simple approximation and setting $f_{\rm xc}^{(2)} = 0$ one arrives at the so-called random phase approximation (RPA) [29, 30], which is well known to fail in the determination of the absorption spectra of insulators, as we now demonstrate with some specific examples. There exists a plethora of approximations for the exchange-correlation kernel. In the following section we only discuss those functionals that have been used in recent years for the study of extended systems. All the results presented in the following section are calculated using the full-potential linearized augmented plane wave method [37], implemented within the Elk code [38]. The ground-state of all materials is determined using LDA for the xc potential and a k-point mesh of $25 \times 25 \times 25$ is used to ensure convergence.

5.1 Random Phase Approximation

In Fig. 1 the absorption spectra for small (Si), medium (diamond), and large band-gap (LiF and Ar) insulators are shown. These spectra are in the long wavelength (i.e. $\mathbf{q} \to 0$) limit. It is clear from Fig. 1 that the RPA results obtained using (31) are shifted to higher energy with respect to the experimental data for Si and diamond. For Si the first peak (E_1) is also suppressed. For LiF and Ar the RPA results are a disaster; the main peak at the onset of the spectra in the experimental data is absent in the RPA results. The reason for these dramatic discrepancies between the experiments and theory were later identified to be the missing electron–hole interactions; the RPA in diagrammatic terms is the sum of the bubble diagrams to infinite order and does not include any interaction between the electron and the hole propagators. In a realistic situation, however, an optically induced excitation of an electron leaves behind a hole and this electron and hole can then form a bound electron–hole pair called the exciton. The presence of excitonic physics shows up as the shifting down (to lower frequencies) of the spectral weight, as compared to RPA

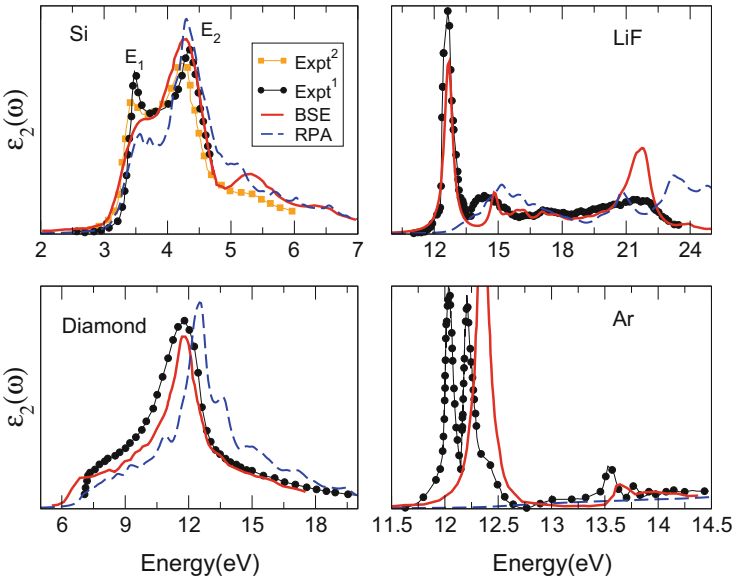

Fig. 1 Imaginary part of the dielectric tensor (ε_2) as a function of photon energy (in eV). Experimental data are taken from the following sources: LiF from [39], Ar from [40], Si from [41, 42], and diamond from [43]. The results for BSE and the RPA are obtained using the Elk-code [38]

results, in Si and diamond and in the appearance of a strong excitonic peek within the band-gap in LiF and Ar.

The many-body perturbation theory approach to include excitonic effects in the absorption spectra is to solve the BSE [44–48]. Appendix 1 of this book gives the details of this method. The results obtained using the BSE are also included in Fig. 1 and, as expected, are in excellent agreement with the experimental data.

5.2 *Adiabatic Local Density Approximation*

Choosing the local density approximation (LDA) for the time-dependent xc-potential in (23) leads to the adiabatic LDA kernel (ALDA kernel) [14]:

$$f_{\mathrm{xc}}^{\mathrm{ALDA}}(\mathbf{r},\mathbf{r}',t-t') = \delta(\mathbf{r}-\mathbf{r}')\delta(t-t')\frac{\delta v_{\mathrm{xc}}^{\mathrm{ALDA}}(\mathbf{r},t)}{\delta\rho(\mathbf{r}',t')}, \tag{35}$$

which is local in space and local in time and hence does not contain any memory effects. In Fig. 2 we show the results for the absorption spectra obtained using the ALDA. The results are not in good agreement with experiments, and in fact show

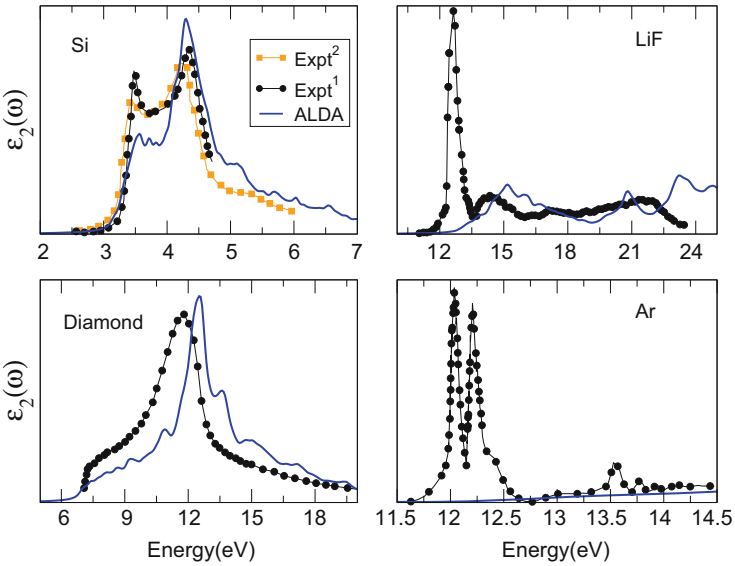

Fig. 2 Imaginary part of the dielectric tensor (ε_2) as a function of photon energy (in eV). Experimental data are taken from the following sources: LiF from [39], Ar from [40], Si from [41, 42], and diamond from [43]. The results for the ALDA are obtained using the Elk-code [38]

very little improvement over the RPA results. The form of the ALDA indicates that it is bound to fail in the long wavelength limit; it can be shown that in this limit χ_s (or χ_{gc}) vanishes as $\mathbf{q}^2$. From (33) it is also clear that $f_{xc}^{(2)}$ must fall off as $1/\mathbf{q}^2$ in order to have any effect on the interacting response function [49]; in the limit $\mathbf{q} \to 0$ the product of χ_{gc} and $f_{xc}^{(2)}$ will vanish for any $f_{xc}^{(2)}$ which falls off slower than $1/\mathbf{q}^2$. This also explains why the ALDA gives essentially the same results (with small differences due to local field effects) as the RPA in the $\mathbf{q} \to 0$ limit.

5.3 *Long-Range Kernel*

Based on this knowledge, a long-range (LR) functional was designed with the form [50, 51]

$$f_{xc}^{LR}(\mathbf{G}_3, \mathbf{G}_2, \mathbf{q}, \omega) = -\frac{\alpha}{|\mathbf{G}+\mathbf{q}|^2}\delta(\mathbf{G}-\mathbf{G}'), \tag{36}$$

where α is a material-dependent parameter. In [51] an empirical formula was proposed for determining α:

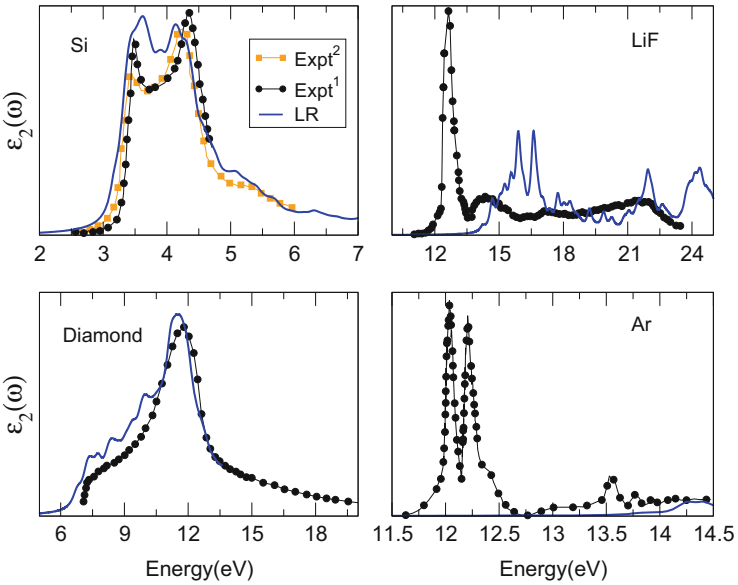

Fig. 3 Imaginary part of the dielectric tensor (ε_2) as a function of the photon energy (in eV). Experimental data are taken from the following sources: LiF from [39], Ar from [40], Si from [41] and [42], and diamond from [43]. The results for the LR kernel are obtained using the Elk-code [38]. The following values of α were used: 0.17 for Si, 0.597 for diamond, 2.14 for LiF, and 2.55 for Ar

$$\alpha = 4.615\varepsilon^{-1}(\mathbf{G} = 0, \mathbf{G}' = 0, \mathbf{q} = 0, \omega = 0) - 0.213. \tag{37}$$

In Fig. 3 we present the results obtained using the long-range kernel (results for many more materials can be found in [51, 52]). This kernel has the correct $\mathbf{q} \to 0$ limit and the results for Si and diamond are in good agreement with experiments. However, the spectra for LiF and Ar show no improvement, with the excitonic peak still missing. For these two materials, one could just abandon (37) and simply choose a value of α which reproduces the correct experimental spectrum. Even though such a choice of α makes the spectra for Ar and LiF close to the experimental data, it takes away the elegance of the ab initio and predictive nature of TDDFT.

5.4 Bootstrap Kernel

Another kernel that has been designed on the basis of the correct $\mathbf{q} \to 0$ behavior of f_{xc} and is fully ab initio in nature is the so-called bootstrap kernel [36, 53]. The name of this kernel derives from the procedure used to calculate the kernel from the following equations:

$$\varepsilon^{-1}(\mathbf{q},\omega) = 1 + \chi_{\mathrm{gc}}(\mathbf{q},\omega)V_{\mathrm{cl}}\left[1 - \left(V_{\mathrm{cl}} + f_{\mathrm{xc}}^{\mathrm{boot}}(\mathbf{q},\omega)\right)\chi_{\mathrm{gc}}(\mathbf{q},\omega)\right]^{-1} \tag{38}$$

with

$$f_{\mathrm{xc}}^{\mathrm{boot}}(\mathbf{q},\omega) = \frac{\varepsilon^{-1}(\mathbf{q},\omega=0)}{\chi_{\mathrm{gc}}^{00}(\mathbf{q},\omega=0)} \tag{39}$$

and all the quantities in this equation are matrices in reciprocal lattice space, as indicated in (31) and (32), but here we suppress the $\mathbf{G}$ indices for notational simplicity. χ^{00} indicates the head of the gap-corrected Kohn–Sham response function, i.e., the $\mathbf{G} = \mathbf{G}' = 0$ component. This coupled set of equations is solved by first setting $f_{\mathrm{xc}}^{\mathrm{boot}} = 0$ and then solving (38) to obtain ε^{-1}. This is then "bootstrapped" in (39) to find a new $f_{\mathrm{xc}}^{\mathrm{boot}}$, and the procedure is repeated until self-consistency between the two equations at $\omega = 0$ is achieved. The results obtained using the bootstrap kernel are presented in Fig. 4. For Si the bootstrap results show that the spectral weight is redistributed and, corresponding to experiment, an enhancement in the E_1 peak is observed. For diamond, the bootstrap procedure correctly leads to an enhancement of the shoulder at low photon energies. The spectral weight is shifted to lower energies, and the whole spectrum is in near perfect agreement with experiment. For LiF and Ar as well, the strong excitonic peak below the band-gap is reproduced by the bootstrap kernel, though it is shifted to higher frequencies with respect to the experimental data.

At this point it is important to mention that in the $\mathbf{q} \to 0$ limit the $\mathbf{G} = \mathbf{G}' = 0$ component of $f_{\mathrm{xc}}^{(2)}$ is the most important one, and hence the bootstrap procedure can be thought of as a self-consistent method for obtaining the system-dependent parameter α of the LRC.

Even though the bootstrap kernel reproduces the main excitonic peak in Ar, it fails to reproduce the so-called Rydberg series of excitons [54]. Since an exciton is a bound electron–hole pair, it has excited states similar to those of a hydrogen atom. For very wide band-gap materials, like the noble gas solids, a Rydberg series can be seen in the experimental spectra, just below the band-gap, while for the case of small band-gap materials these excited states merge with the continuum part of the spectrum and are difficult to resolve. The failure of the bootstrap kernel for capturing the Rydberg series lies in the fact that the essential feature of any $f_{\mathrm{xc}}^{(2)}$, which would enable it to capture the Rydberg series, is its frequency dependence. However, the bootstrap kernel is not frequency-dependent and hence can only reproduce a single peak below the band-gap.

At this point it is an interesting question to ask – what is the effect of the choice of the ground-state xc potential on the absorption spectra? In other words, would improving χ_{gc} improve the final results or have we reached the limit of accuracy of the bootstrap procedure. In order to shed light on this one can use a computationally expensive but much more accurate xc functional, namely the exact-exchange potential or the so-called optimized effective potential (OEP) [55–63]. This functional has been shown to produce better band-gaps in particular and full band

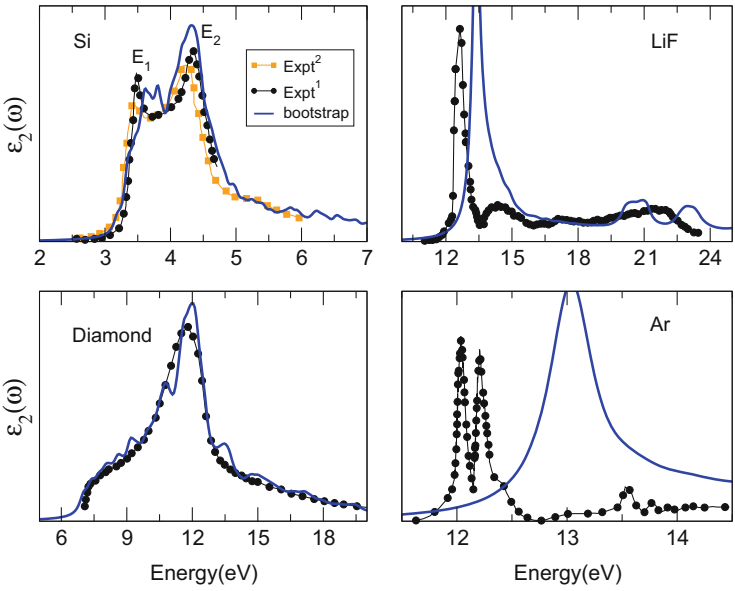

Fig. 4 Imaginary part of the dielectric tensor (ε_2) as a function of photon energy (in eV). Experimental data are taken from the following sources: LiF from [39], Ar from [40], Si from [41, 42], and diamond from [43]

structure in general for simple solids [57, 60]. To demonstrate the effect of more accurate OEP band structure on the optical absorption spectra, we choose our best example, diamond (here the absorption spectra calculated on top of LDA ground-state is already in excellent agreement with experiments) and the worst example, LiF (here the spectra calculated on top of the LDA ground-state is not in very good agreement with experiments). The results are shown in Fig. 5. It is clear that a more accurate ground-state leads to excellent absorption spectra for LiF, while the results do not change very much for diamond and are still in very good agreement with experiments. This indicates that either the ground-state needs to be improved by means of *GW*-like calculations or one needs to find a better approximation for $f_{\mathrm{xc}}^{(1)}$ within the framework of TDDFT.

5.5 *Nanoquanta Kernel*

A kernel for TDDFT can also be derived from many-body perturbation theory, essentially by identifying the BSE expression for the optical spectrum with the one from TDDFT. This kernel is called the Nanoquanta kernel [50, 66] (named after the Nanoquanta consortium where it was found) and has the correct $1/\mathbf{q}^2$ behavior in the

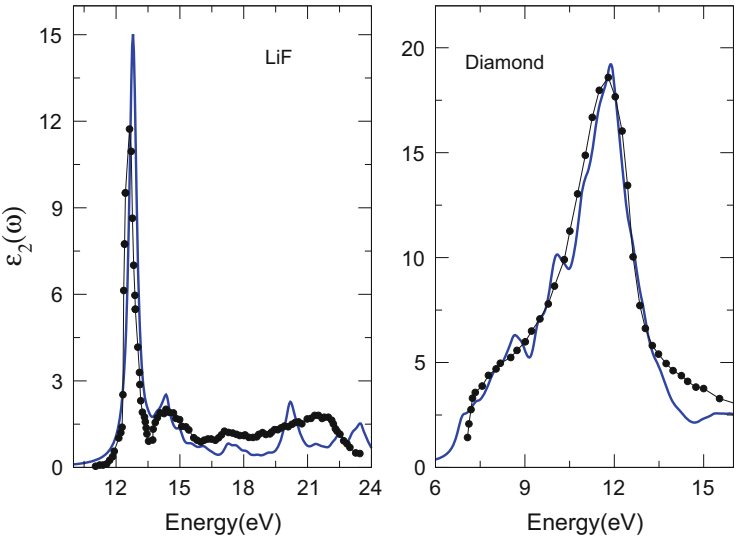

Fig. 5 Imaginary part of the dielectric tensor (ε_2) as a function of photon energy (in eV). The bootstrap calculations are performed starting from OEP band structure

long wavelength limit. The form of the kernel is rather complicated. It is given by the following three equations:

$$\chi_s(\mathbf{G},\mathbf{G}_1,\omega) f_{xc}^{NQ}(\mathbf{G}_1,\mathbf{G}_2,\omega)\chi_s(\mathbf{G}_2,\mathbf{G}',\omega) = \sum_{i,i',j,j'} \frac{\psi_j(\mathbf{G})\psi_i(\mathbf{G})}{\epsilon_j-\epsilon_i-\omega} F_{ij,i'j'}^{BSE} \frac{\psi_{j'}^*(\mathbf{G}')\psi_{i'}^*(\mathbf{G}')}{\epsilon_{j'}-\epsilon_{i'}-\omega}, \tag{40}$$

where

$$F_{ij,i'j'}^{BSE} = \int d^3r d^3r' \psi_i(\mathbf{r})\psi_{i'}(\mathbf{r}) W(\mathbf{r},\mathbf{r}',\omega=0)\psi_j^*(\mathbf{r}')\psi_{j'}^*(\mathbf{r}'), \tag{41}$$

and where W is the screened Coulomb interaction:

$$W(\mathbf{r},\mathbf{r}',\omega=0) = \frac{\varepsilon^{-1}(\mathbf{r},\mathbf{r}',\omega=0)}{|\mathbf{r}-\mathbf{r}'|} \tag{42}$$

The results obtained using the Nanoquanta kernel are shown in Fig. 6 and it is clear that the results are of the same quality as those obtained using BSE and are in excellent agreement with experiments. This is expected as the kernel is directly derived from the BSE itself. The only disadvantage to this is that, like solving BSE, the calculation of the Nanoquanta kernel is computationally very expensive.

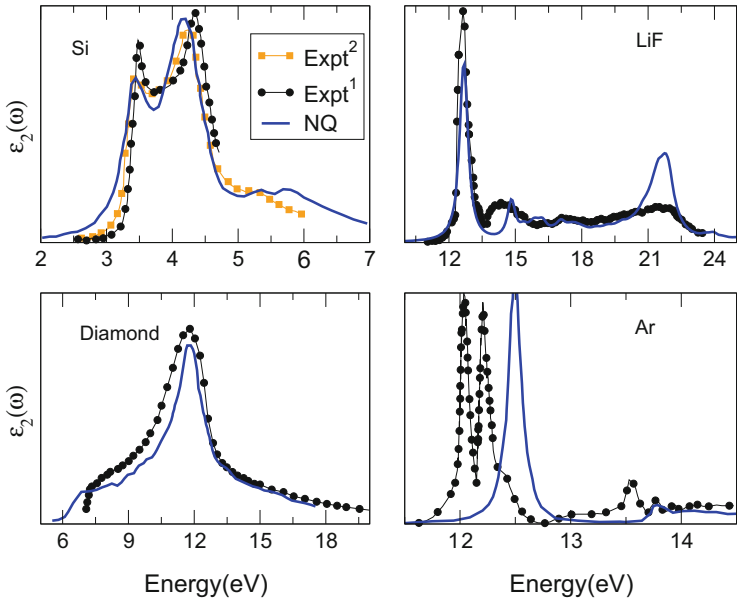

Fig. 6 Imaginary part of the dielectric tensor (ε_2) as a function of photon energy (in eV). Experimental data are taken from the following sources: LiF from [39], Ar from [40], Si from [41, 42], and diamond from [43]. The results for the Nanoquanta kernel are taken from [35, 50, 64–66]

6 Electron Energy Loss Spectra

In contrast to the optical absorption spectra in the long wavelength limit, the EELS at finite values of $\mathbf{q}$ (away from the Γ-point) can be accurately treated [68, 69] by the ALDA. This is a surprising result because ALDA does not have the $1/|\mathbf{q}|^2$ dependence and hence indicates that the EELS away from the Γ-point may not necessarily require the xc kernel to have this form. This then raises an interesting question about the validity of the kernels which accurately treat the $\mathbf{q} \rightarrow 0$, for finite values of $\mathbf{q}$. In order to shed light on this issue in the following we plot the EELS for LiF and diamond for various values of $\mathbf{q}$ in Fig. 7.

Three different values of $\mathbf{q}$ in the $\Gamma - X$ direction are presented for LiF. The bootstrap kernel well reproduces the experimental data and the BSE results which show three main peaks at $\mathbf{q} = 0.23\ \Gamma X$. On going from 0.23 to 0.48 ΓX the plasmonic peak at 25 eV gets smaller in magnitude, a feature which is again well captured by the bootstrap kernel. Experiments, BSE, and bootstrap results show that outside the first BZ (for $\mathbf{q} = 1.50\ \Gamma X$) the EELS will be highly suppressed. These results indicate that the bootstrap kernel captures the change in $-\ \mathrm{Im}[\varepsilon^{-1}]$ as a function of $\mathbf{q}$ very well. We note, however, that the magnitude of the peaks is slightly overestimated by the bootstrap kernel and, for small energies, the peaks are blue shifted by ~0.75 eV compared to experiment. This shifting of the excitonic

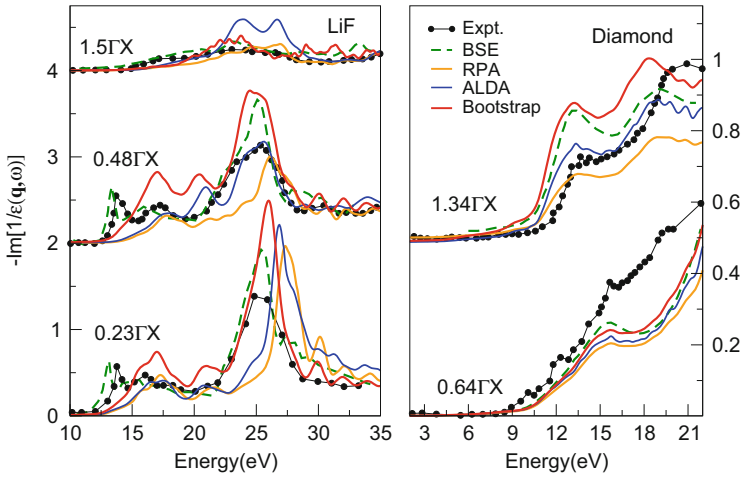

Fig. 7 The EELS for different values of **q** (*indicated in the figure*) as a function of energy in eV for LiF and diamond. The results obtained using the bootstrap kernel are shown with *full lines*, the experimental data (from [67]) with *dots*, the BSE results (also taken from [67]) with *dashed lines*, and the ALDA results with *thin* (*blue*) *lines*. The results for different values of **q** are shifted vertically for clarity

peaks to higher frequencies and the overestimation of their magnitude was also a feature of the absorption spectra in the long wavelength limit (see Fig. 4). The RPA results are shifted to higher frequencies compared to the BSE and the experimental data. The ALDA results are an improvement over RPA. However, the ALDA results disagree with the BSE data for large values of **q**.

For diamond, the magnitude of the EELS obtained using the bootstrap kernel is overestimated compared to the experiments. A similar overestimation is also seen in the BSE results. In fact, we find that the results obtained using the bootstrap kernel are in very good agreement with the BSE results. As in the case of LiF, the ALDA and RPA results disagree with the BSE data for larger values of **q**. It is important to point out that, unlike in the $\mathbf{q} \to 0$ limit, for finite values of **q** the matrix character of $f_{xc}^{(2)}$ is crucial. If one ignores the matrix nature of $f_{xc}^{(2)}$ and uses only the head of $f_{xc}^{(2)}$, i.e., long-range kernel, the results are significantly worse [36].

7 Summary and Perspectives

To summarize in this chapter, we have detailed the Runge–Gross theorem for TDDFT and presented the time-dependent Kohn–Sham equations as a practical prescription for evaluating the time-dependent density. We also derived the exact linear response function in terms of the non-interacting Kohn–Sham response function and the exchange-correlation kernel f_{xc}. The strengths and weaknesses of

present-day approximate kernels were illustrated for small (Si), medium (diamond), and large (LiF and Ar) band-gap insulators. The bootstrap kernel, which is a functional of the dielectric function and therefore indirectly of the density, is a parameter-free kernel which was shown to capture the excitonic response in solids with an accuracy rivaling that of the BSE.

As far as future developments are concerned, there are several directions in which TDDFT within linear response and beyond is likely to expand and some of them we list below:

1. In nature, excitons, which are bound electron–hole pairs similar to a hydrogen atom, show a hydrogenic-like Rydberg series. In very large band-gap materials like Ar, Ne, and Kr this manifests itself as several peaks in the optical absorption spectra below the fundamental gap. To capture the whole Rydberg series of excitons within TDDFT, the xc kernel must be frequency-dependent. For now there does not exist any kernel capable of capturing this physics. One of the future developments in the field of xc kernel design would certainly be in this direction.
2. Within the last 15 years, a new field of research concerned with the ultrafast manipulation processes of ferromagnetic materials has emerged. Several experiments have demonstrated that demagnetization or spin-reorientation processes can be induced by femtosecond laser pulses [70, 71]. Despite intensive experimental research and theoretical efforts, the underlying mechanisms driving the ultrafast magnetism are not yet really understood and are the subject of heavy discussions at the moment. In order to shed light on this, realtime propagation of the time-dependent KS equations for magnetic periodic systems is expected in the near future.
3. TDDFT in its current formulation treats the electromagnetic field classically. This prevents the description of phenomena in which the quantum nature of light is relevant. For example, the process of lazing a material relies on the emission of photons and hence its ab initio description can only be properly achieved by means of a photon density alongside the standard density of electrons. Another example is that of cavity quantum electrodynamics (QED) where electrons interact just with a few modes of the electromagnetic field which can only be correctly described by excitation of the quantized field. Both of these rather important phenomena require the treatment of light as a quantum phenomenon and hence an extension of TDDFT to QED is necessary [72, 73]. Several advances in this direction are imminent.
4. The rapid miniaturization of electronic devices motivates research interests in quantum transport [74–76]. TDDFT combined with a non-equilibrium Green's function approach [77–79] promises realtime simulations of ultrafast electron transport through realistic electronic devices. However, what is required to do a realistic calculation of a device using such an xc functional that incorporates the discontinuities with respect to particle number [80, 81]? Designing of new functionals of this kind will also be an important task for future development.

5. Intermediate timescales of a few hundred femtoseconds for which both electron and nuclear dynamics are relevant require a more sophisticated treatment than Ehrenfest dynamics. It is possible to perform a Born–Oppenheimer-like factorization of the full electron-nuclear wavefunction, which is nevertheless exact [82, 83]. Such a factorization may be made practicable by using it in conjunction with TDDFT.

References

1. Hohenberg P, Kohn W (1964) Phys Rev 136:B864
2. Kohn W, Sham LJ (1965) Phys Rev 140:A1133
3. Jones RO, Gunnarsson O (1989) Rev Mod Phys 61:689
4. Perdew JP, Zunger A (1981) Phys Rev B 23:5048
5. Perdew JP, Burke K, Ernzerhof M (1996) Phys Rev Lett 77:3865
6. Perdew JP, Burke K, Ernzerhof M (1997) Phys Rev Lett 78:1396(E)
7. Perdew JP, Burke K (1996) Int J Quantum Chem 57:309
8. Kotliar G, Savrasov SY, Haule K, Oudovenko VS, Parcollet O, Marianetti CA (2006) Rev Mod Phys 78:865
9. Sim F, St-Amand A, Papai I, Salahub DR (1992) J Am Chem Soc 114:4391
10. Godby RW, Schlüter M, Sham LJ (1987) Phys Rev B 36:6497
11. Hedin L (1965) Phys Rev 139:A796
12. Salpeter EE, Bethe HA (1951) Phys Rev 84:1232
13. Runge E, Gross EKU (1984) Phys Rev Lett 52:997
14. Zangwill A, Soven P (1980) Phys Rev Lett 45:204
15. Gross EKU, Kohn W (1985) Phys Rev Lett 55:2850
16. Gross EKU, Kohn W (1986) Phys Rev Lett 57:923
17. van Leeuwen R (2001) Int J Mod Phys B 15:1969
18. Gross EKU, Kohn W (1990) Adv Quant Chem 21:255
19. Kohn W (1999) Rev Mod Phys 71:1253
20. Ankudinov AL, Nesvizhskii AI, Rehr JJ (2003) Phys Rev B 67:115120
21. Kootstra F, de Boeji PL, Leeuwen R, Snijders JG (2002) Reviews in modern quantum chemistry: a celebration of the contributions of Robert Parr. World Scientific, Singapore, pp 1155–1185
22. Gross EKU, Burke K (2006) Lecture notes in physics. Springer, Heidelberg, pp 1–12
23. Petersilka M, Gossmann UJ, Gross EKU (1996) Phys Rev Lett 76:1212
24. Bertsch GF, Iwata JI, Rubio A, Yabana K (2000) Phys Rev B 62:7998
25. Castro A, Marques MAL, Alonso JA, Rubio A (2004) J Comp Theoret Nanoscience 1:231
26. Yabana K, Sugiyama T, Shinohara Y, Otobe T, Bertsch GF (2012) Phys Rev B 84:045134
27. van Leeuwen R (1999) Phys Rev Lett 82:3863
28. Ehrenreich H, Cohen M (1959) Phys Rev 115:786
29. Adler SL (1962) Phys Rev 126:413
30. Wiser N (1963) Phys Rev 129:62
31. Del Sole R, Fiorino E (1984) Phys Rev B 29:4631
32. Maddocks NE, Godby RW, Needs RJ (1994) Europhys Lett 27:681
33. Gurtubay IG, Ku W, Pitarke JM, Eguiluz AG, Larson BC, Tischler J, Zschack P (2005) Phys Rev B 72:125117
34. Weissker HC, Serrano J, Huotari S, Bruneval F, Sottile F, Monaco G, Krisch M, Olevano V, Reining L (2006) Phys Rev Lett 96:237602
35. Marini A, Sole RD, Rubio A (2003) Phys Rev Lett 91:256402
36. Sharma S, Drewhurst JK, Sanna A, Rubio A, Gross EKU (2012) New J Phys 14:053052
37. Singh DJ (1994) Planewaves pseudopotentials and the LAPW method. Kluwer Academic, Boston

38. Dewhurst JK, Sharma S et al (2004) http://elk.sourceforge.net
39. Roessler D, Walker W (1967) J Opt Soc Am 57:835
40. Sonntag B (1976) In: Klein ML, Venables JA (eds) Rare gas solids, vol II. Academic, London, pp 10211117
41. Lautenschlager P, Garriga M, Vina L, Cardona M (1987) Phys Rev B 36:4821
42. Aspnes DE, Studna AA (1983) Phys Rev B 27:985
43. Edwards D, Philipp H (1985) In: Palik ED (ed) Handbook of optical constants of solids. Academic, Orlando
44. Albrecht S, Reining L, Del Sole R, Onida G (1998) Phys Rev Lett 80:4510
45. Benedict LX, Shirley EL, Bohn RB (1998) Phys Rev Lett 80:4514
46. Rohlfing M, Louie SG (1998) Phys Rev Lett 81:2312
47. Rohlfing M, Louie SG (2000) Phys Rev B 62:4927
48. Benedict LX, Shirley EL, Bohn RB (1998) Phys Rev B 57:R9385
49. Gonze X, Ghosez P, Godby RW (1995) Phys Rev Lett 74:4035
50. Reining L, Olevano V, Rubio A, Onida G (2002) Phys Rev Lett 88:066404
51. Botti S, Sottile F, Vast N, Olevano V, Weissker H-C, Reining L, Onida G, Rubio A, Sole RD, Godby RW (2004) Phys Rev B 69:155112
52. Del Sole R, Adragna G, Olevano V, Reining L (2003) Phys Rev B 67:045207
53. Sharma S, Drewhurst JK, Sanna A, Gross EKU (2011) Phys Rev Lett 107:186401
54. Petersilka M, Gross EKU, Burke K (2000) Int J Quantum Chem 80:534
55. Görling A, Levy M (1994) Phys Rev A 50:196
56. Görling A (1996) Phys Rev B 53:7024
57. Städele M, Majewski JA, Vogl P, Görling A (1997) Phys Rev Lett 79:2089
58. Magyar RJ, Fleszar A, Gross EKU (2004) Phys Rev B 69:045111
59. Niquet YM, Gonze X (2004) Phys Rev B 70:245115
60. Städele M, Moukara M, Majewski JA, Vogl P, Görling A (1999) Phys Rev B 59:10031
61. Kotani T (1995) Phys Rev Lett 74:2989
62. Sharma S, Dewhurst JK, Ambrosch-Draxl C (2005) Phys Rev Lett 95:136402
63. Sharma S, Dewhurst JK, Ambrosch-Draxl C, Kurth S, Helbig N, Pittalis S, Shallcross S, Nordström L, Gross EKU (2007) Phys Rev Lett 98:196405
64. Sottile F, Marsili M, Olevano V, Reining L (2007) Phys Rev Lett 76:161103
65. Botti S, Schindlmayr A, Sole RD, Reining L (2007) Phys Rev Lett 76:161103
66. Sottile F, Karlsson K, Reining L, Aryasetiawan F (2003) Phys Rev B 68:205112
67. Caliebe WA, Soininen JA, Shirley EL, Kao C-C, Hämäläinen K (2000) Phys Rev Lett 84:3907
68. Botti S et al (2007) Rep Prog Phys 70:357
69. Weissker H-C, Serrano J, Huotari S, Luppi E, Cazzaniga M, Bruneval F, Sottile F, Monaco G, Olevano V, Reining L (2010) Phys Rev B 81:085104
70. Beaurepaire E, Merle J-C, Daunois A, Bigot J-Y (1996) Phys Rev Lett 76:4250
71. Eschenlohr A, Battiato M, Maldonado P, Pontius N, Kachel T, Holldack K, Mitzner R, Föhlisch A, Oppeneer PM, Stamm C (2013) Nat Mater 12:332
72. Ruggenthaler M, Mackenroth F, Bauer D (2011) Phys Rev A 84:042107
73. Tokatly IV (2013) Phys Rev Lett 110:233001
74. Taylor J, Guo H, Wang J (2001) Phys Rev B 63:245407
75. Brandbyge M, Mozos J-L, Ordejón P, Taylor J, Stokbro K (2002) Phys Rev B 65:165401
76. Stefanucci G, Almbladh C-O (2004) Phys Rev B 69:195318
77. Kurth S, Stefanucci G, Khosravi E, Verdozzi C, Gross EKU (2010) Phys Rev Lett 104:236801
78. Uimonen AM, Khosravi E, Stan A, Stefanucci G, Kurth S, van Leeuwen R, Gross EKU (2011) Phys Rev B 84:115103
79. Khosravi E, Uimonen AM, Stan A, Stefanucci G, Kurth S, Leeuwen R, Gross EKU (2010) Phys Rev B 85:075103
80. Hellgren M, Gross EKU (2012) J Chem Phys 136:114102
81. Hellgren M, Gross EKU (2012) Phys Rev A 85:022514
82. Abedi A, Maitra NT, Gross EKU (2010) Phys Rev Lett 105:123002
83. Abedi A, Agostini F, Suzuki Y, Gross EKU (2013) Phys Rev Lett 110:263001